Nanoscale

PAPER

Direct conversion of multilayer molybdenum trioxide to nanorods as multifunctional electrodes in lithium-ion batteries†

Mohammed Aziz Ibrahem,[abc] Feng-Yu Wu,[g] Desalegn Alemu Mengistie,[bde] Chia-Seng Chang,[f] Lain-Jong Li[g] and Chih Wei Chu*[dh]

In this study we prepared molybdenum trioxide (MoO₃) nanorods having average lengths of 0.5–1.5 μm and widths of approximately 100–200 nm through a one-step mechanical break-down process involving favorable fracturing along the crystal direction. We controlled the dimensions of the as-prepared nanorods by applying various imposing times (15–90 min). The nanorods prepared over a reaction time of 90 min were, on average, much shorter and narrower relative to those obtained over 30 min. Evaluations of lithium-ion storage properties revealed that the electrochemical performance of these nanorods was much better than that of bulk materials. As cathodes, the nanorods could deliver a high specific capacity (>315 mA h g⁻¹) with losses of less than 2% in the first cycle at a rate of 30 mA g⁻¹; as anodes, the specific capacity was 800 mA h g⁻¹ at a rate of 50 mA g⁻¹. Relative to α-MoO₃ microparticles, these nanorods displayed significantly enhanced lithium-ion storage properties with higher reversible capacities and better rate performance, presumably because their much shorter diffusion lengths and higher specific surface areas allowed more-efficient insertion/deinsertion of lithium ions during the charge/discharge process. Accordingly, enhanced physical and/or chemical properties can be obtained through appropriate nanostructuring of materials.

Introduction

Molybdenum trioxide (MoO₃) is an important transition metal oxide because of its rich chemistry, associated with multiple valence states, and its high thermal and chemical stability. It occurs as the rare mineral molybdite in three different anhydrous crystalline polymorphs: thermodynamically stable orthorhombic α-MoO₃, metastable monoclinic β-MoO₃ having a rhenium trioxide (ReO₃)-type structure, and metastable high-pressure phase MoO₃-II.[1,2] The β phase generally transforms into the more-stable, layered α-MoO₃ phase at temperatures above 350 °C.[3,4] The crystal structure of α-MoO₃ is anisotropic; each layer comprises two sublayers, with the octahedra along the [001] and [100] directions sharing the corner of each layer.

Alternatively, these layered sheets are held together vertically in the [010] direction by weak van der Waals interaction, while the internal bonds in the octahedra are dominated by covalent and ionic bonds (Fig. S1, ESI†).[1,5]

The lamellar structures and facile formation of intercalated states with high activity[6,7] make MoO₃ species excellent candidates for use in many important applications, including gas sensors,[8] recording materials,[9] lubricants,[10] photochromic materials,[11] displays,[12] organic solar cells,[13] and catalysis.[14] Furthermore, MoO₃ materials are promising for energy storage because their layered structures allow intercalation and storage of a large number of ions within their lattice, providing the facile access and high-energy release rates required for industrial devices.[3] MoO₃ is also a promising electrode material in lithium-ion batteries (LIBs) because of its high lithium storage capacity, widespread availability, and intrinsically high safety (avoiding the formation of hazardous lithium dendrite).[15,16] When employed as cathode materials in LIBs, MoO₃ can deliver capacities of 200–300 mA h g⁻¹ between 1.5 and 3.5 V on the basis of an intercalation mechanism.[17] In contrast, α-MoO₃ has attracted much less attention as an anode material because of its poor electrochemical properties caused by intrinsic sluggish kinetics for redox conversion reactions and large structure variations upon lithium insertion/extraction, despite a theoretical capacity as high as 1117 mA h g⁻¹.[15,17]

[a]Department of Physics, National Taiwan University, Taipei 106, Taiwan

[b]Nanoscience and Technology Program, Taiwan International Graduate Program, Academia Sinica, Taipei 115, Taiwan

[c]Department of Physics, Faculty of Science, University of Duhok, Duhok, Iraq

[d]Research Center of Applied Science, Academia Sinica, Taipei 115, Taiwan

[e]Institute of Technology, Bahir Dar University, Bahir Dar, Ethiopia

[f]Institute of Physics, Academia Sinica, Taipei 115, Taiwan

[g]Institute of Atomic and Molecular Sciences Academia Sinica, Taipei 10617, Taiwan

[h]Department of Photonics, National Chiao Tung University, Hsinchu 300, Taiwan. E-mail: gchu@gate.sinica.edu.twa

† Electronic supplementary information (ESI) available. See DOI: 10.1039/c4nr00692e

To further enhance the capability of nanostructured materials for energy conversion and storage, new mechanisms and structures will be necessary to ensure the availability of nanomaterials in large quantities with well-defined structures and to control the fabrication of these materials into functional devices. Through control of nanostructure morphologies, micro/nanostructured architectures, hollow architectures, and the manipulation of surface chemistry, it is believed that the many present obstacles affecting energy conversion devices can be overcome, thereby enhancing their performance. MoO_3 can be engineered into several low-dimensional nanostructures, including nanowires,[18] single-walled nanotubes,[19] nanorods,[20] nanofibers,[17] nanoparticles,[13] nanobelts,[3] and nanoribbons,[21] for use as electrodes having excellent ion and electron transport rates and large surface-to-volume ratios. Among these nanostructures, rod or belt-like α-MoO_3 structures have attracted high interest because the single-crystalline nature serves well as a representation of the layered structure and anisotropic growth.[3,22] The synthesis of pure α-MoO_3 nanorods having controlled aspect ratios has, however, been difficult to achieve because approaches involving hydrothermal, solvothermal, and vapor-deposition techniques have required high temperatures, high vacuum, and/or high pressure in the presence of a carrier gas (e.g., Ar or O_2).

Herein, we report a rapid but effective one-step approach for breaking down α-MoO_3 microparticles into nanorods in high yield through control over the imposing time. This efficient preparation provides pure α-MoO_3 nanorods after a fracturing time of only 90 min. More importantly, this solution-based method has several advantages in terms of both processing and properties. The processing is extremely simple, rapid, and reproducible in any laboratory; it is insensitive to ambient conditions; it consumes low amounts of energy; and it can potentially be scaled up to give large quantities (grams) of exfoliated materials (Fig. S2, ESI†) in dispersions that exhibit high stability over long periods of time (at least three months; Fig. S3, ESI†). Most importantly, the mechanical interactions during processing affect the electronic properties of dispersed nanomaterials only slightly. Furthermore, the resultant nanorods can be easily applied as multifunctional (cathode or anode) electrodes in LIBs, with specific capacities comparable with those reported previously.

Experimental section

Material preparation

The conversion process used to prepare MoO_3 nanorods is presented in Scheme 1. Pristine MoO_3 powder (99.5%, Sigma-Aldrich) was mixed with pure isopropanol alcohol (IPA, Sigma-Aldrich) at a concentration of 5 wt%. Mechanical commuting through bead-milling in a homemade grinder was performed for different periods of time. The stirrer comprised of three perforated discs mounted on a drive shaft. Approximately 60% of the container was filled with micro-sized beads (zirconia beads; size: 100 μm; density: ca. 5.95 g cm^{-3}); the remaining volume contained a suspension of particles to be ground. The beads and the suspension were strongly stirred using a central

rotating agitator, typically at speeds ranging from 1000 to 3000 rpm (the peripheral speed of the rotor was fixed at 2000 rpm). The resultant dark-blue dispersion was purified without any contamination of zirconia beads because these beads were of high density and precipitated very rapidly to the bottom of the container after grinding.

Characterization

The dispersion was diluted tenfold with IPA; drops of the solution were placed on a holey carbon-coated copper grid (Lacey Carbon Type-A 300 mesh copper grids; TED Pella) or Si/SiO_2 and then dried in air at 70 °C prior to characterization using transmission electron microscopy (TEM, JEM 2100F), scanning electron microscopy (SEM, FEI Nova200), tapping-mode atomic force microscopy (AFM, Veeco di Innova) with X-ray photoelectron spectroscopy (XPS, PHI 5000 Versa Probe scanning ESCA microprobe), and Raman spectroscopy (NT-MDT confocal Raman microscopic system; exciting laser wavelength: 514 nm; laser spot-size: 0.5 μm). Powders before and after grinding were characterized using X-ray powder diffraction (XRD, PANalytical). The specific surface area measurements were determined using a Digisorb 2006 surface area, pore volume analyzer-Nova Quanta Chrome Corporation instrument using multipoint BET adsorption.

Electrochemical test

MoO_3 powders were used as cathode materials in lithium-ion batteries. MoO_3 powders were mixed with Super P and PVDF at a ratio of 8 : 1 : 1 in N-methyl-2-pyrolidinone (NMP, Macron Chemical) and subjected to ball-milling to form the slurry. The slurry was coated on Al foil and dried at 110 °C for 4 h and then baked in a vacuum oven at 110 °C for 4 h. The coin cells were assembled with cut cathodes, a separator (Celgard 2600), and an electrolyte in a glove box under an Ar atmosphere. The electrolyte (1 M $LiPF_6$) was dissolved in a mixture of solvents: ethyl methyl carbonate, dimethyl carbonate, and vinylene carbonate (1 : 1 : 1). The test voltage was within the range from 3.8 to 1.5 V.

Results and discussion

Fig. 1a displays the crystallographic structure and phase purity of the MoO_3 samples, as determined using X-ray diffraction (XRD). All the recorded diffraction peaks for the sample before and after imposing can be indexed mainly to an orthorhombic phase of MoO_3, in good agreement with literature values (JCPDS #35-0609; a = 0.3963 nm; b = 1.3856 nm; c = 0.3697 nm). The absence of notable impurity peaks suggests high purity for the α-MoO_3 product prepared using our new method. The stronger intensities of the (020), (040), and (060) diffraction peaks suggest highly anisotropic growth of these nanostructures.[15,23,24] Moreover, the nearly identical diffraction angles (2θ) for the bulk material and the nanorods indicate the same degrees of crystallinity; the lower intensity and broadening of the peaks after grinding is consistent with smaller lateral sizes.[25] Raman spectroscopy further confirmed the formation of the MoO_3 nanorods. The Raman spectrum ($\lambda_{excitation}$ = 514 nm) in Fig. 1b
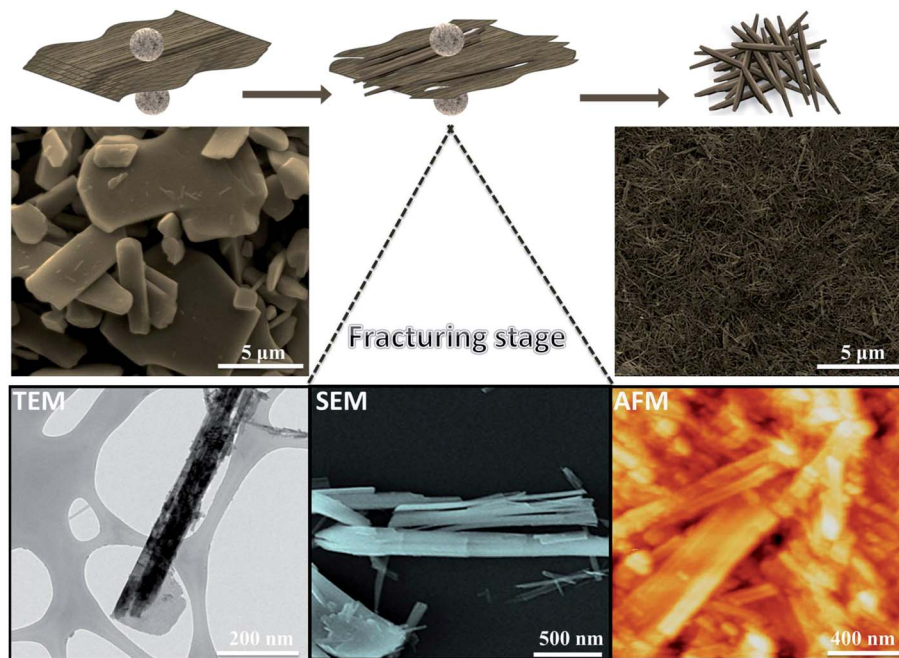
Scheme 1 Schematic representation of the conversion process, with corresponding microscopy images: a 3D network of bulk MoO_3 micro-particles is converted to one-dimensional nanorods under the impact and friction of beads. The fracturing process in the intermediate stage is clearly evident: sheets have been fractured along the axial direction to form parallel nanorods.
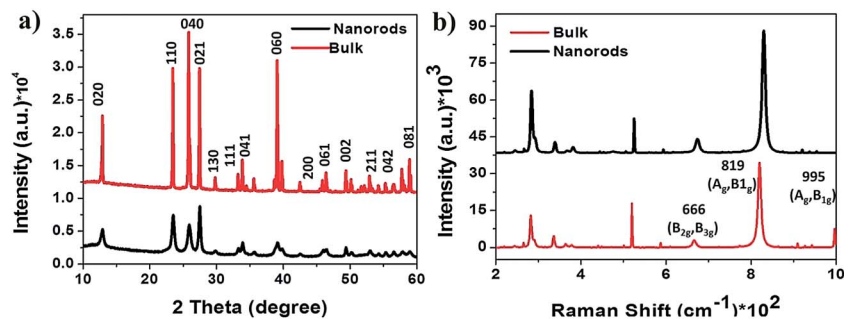

Fig. 1 Structural analysis of MoO_3: (a) powder XRD patterns of bulk and nanorod forms of MoO_3 (orthorhombic phase: JCPDS #35-0609; $a = 0.3963$ nm; $b = 1.3856$ nm; $c = 0.3697$ nm). (b) Raman spectra ($\lambda_{excitation} = 514$ nm) of bulk and nanorod forms of MoO_3.

features the main bands of α-MoO_3: a signal at 995 cm^{-1} that we assign to the terminal oxygen atom (Mo–O) stretching mode;[26] a signal at 666 cm^{-1} representing the edge-sharing, triple-coordinated oxygen [Mo(3)–O] stretching mode; for bulk α-MoO_3, the chain of octahedral MoO_6 adjoined at the corners by a double-coordinated oxygen (Mo–O–Mo) stretching mode is assigned to the dominant 821 cm^{-1} peak. Whereas for nanorods the stretching mode adjoined at 819 cm^{-1} with blue shift; and signals in the range 100–500 cm^{-1} resulting from various other vibrational modes (*e.g.*, fracturing, twisting, bending).[27,28] In addition, the peaks related to the nanorods were broadened and had intensities much lower than those of the bulk material, similar to the effect in the XRD patterns. Such behavior of broadening and blue shift might be due to the large lattice expansion and structural distortion related to interlayer intercalation. Furthermore, the variation of the stoichiometry within the

sample series is rather than smaller, only minor variation of the Raman band of the localized vibration, *e.g.* 666, 821 or 995 bands are expected. In addition, different degrees of crystallization of the sample, a lower oxygen/metal ratio, and a broadening of the intense bands at 821 and 995 should be expected.[27,29]

We employed transmission electron microscopy (TEM) imaging and diffraction analysis to determine the crystal structure of an individual nanorod. Fig. 2a and S6a–c (ESI)† present TEM images of nanorods with various surface morphologies and having a length of a few hundred nanometers and a width of approximately >50 nm, matching well the dimensions observed in the scanning electron microscopy (SEM) and tapping-mode atomic force microscopy (AFM) images in Fig. 2. High-resolution transmission electron microscopy (HRTEM) revealed (Fig. 2b) 2D lattice fringes with a thick (*ca.* 5 nm) coating-like amorphous structure at the rod's
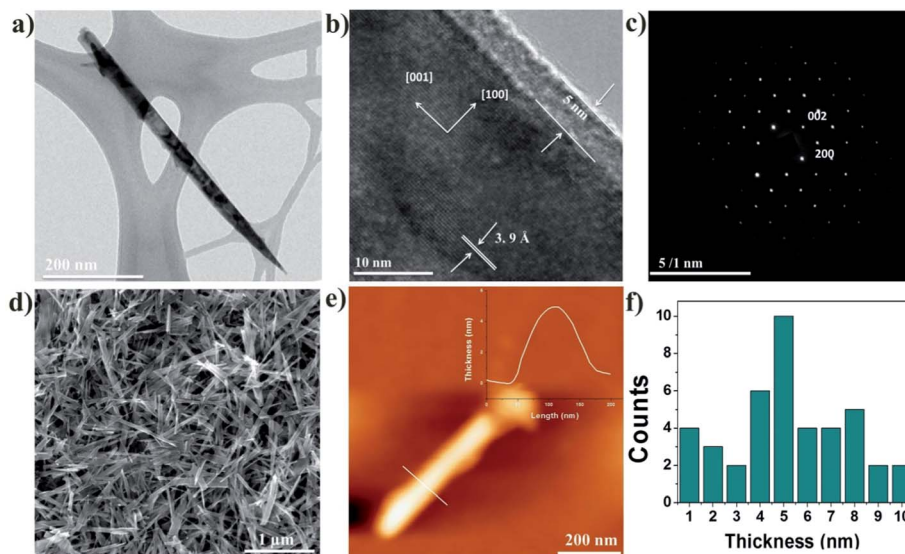
Fig. 2 (a) TEM image of an individual MoO₃ nanorod. (b) HRTEM image of a typical nanorod. (c) SAED pattern of the nanorod in (b). (d) SEM image of nanorods. (e) AFM height image of a typical nanorod; inset: corresponding height profile. (f) Thickness histogram of 42 different nanorods.

edge. This can be attributed to the fracturing process along the energy minimized direction (here is (001)), since α-MoO₃ is a 2D layered material, therefore when the layer is ruptured it will produce different crystal deformations on the edge, the stacking of these deformed edge will produce an amorphous layer on the nanorod's side surface. Selected-area electron diffraction (SAED) provided a pattern appearing as a regular array of diffraction spots along the [100] zone axis of the α-MoO₃ crystal (Fig. 2c), indicating a highly single-crystalline material. The data reveal that the MoO₃ nanorods were structurally uniform, with an interplanar spacing of approximately 0.39 nm, corresponding to the (001) plane,[30] consistent with the XRD patterns (Fig. 1a), and growth along the [001] direction, confirming that no distortion occurred upon flattening and fracturing of these materials. Furthermore, the surfaces of the obtained nanorods were rough, featuring step-like edges, as indicated by the circle point in Fig. S6 (ESI†) as well as in the height profile of the AFM image in the inset of Fig. 2e.

We also used SEM and AFM to characterize the morphologies of the α-MoO₃ nanorods. The SEM panoramic view in Fig. 2d reveals that the sample consisted of entirely uniform nanorods, without impurity particles or aggregates, having lengths of less than 2 μm and uniform widths of 100–200 nm, in contrast to the very thick (>3 μm) and long (>10 μm), disordered, network arrangement of sheets for the bulk α-MoO₃ (Fig. S4, ESI†). AFM images [Fig. 2e and S5 (ESI†)] suggested nanorod dimensions similar to those deduced from the SEM and TEM images, with the majority having an average thickness of less than 10 nm (Fig. 2f).

We employed X-ray photoelectron spectroscopy (XPS), energy dispersion spectroscopy (EDS), and X-ray fluorescence (XRF) to investigate the stoichiometry of the nanorods. We assign the core levels of peaks at binding energies (BEs) of 242.4 ± 0.1 and 235.7 ± 0.1 eV in the XPS spectrum of MoO₃ (Fig. S7, ESI†) to the Mo $3d_{5/2}$ and Mo $3d_{3/2}$ orbitals, respectively, of the

characteristic Mo⁶⁺ oxidation state of MoO₃, with the signal at a BE of 530.2 ± 0.1 eV representing the O 1s orbital.[11,31] From the EDS spectrum in Fig. S8 ESI,† we estimated the atomic ratio of Mo to O in the nanorods to be close to 1 : 3; XRF-based elemental analysis also provided an O-to-M of approximately 1 : 3, suggesting MoO₃ as the empirical formula.

Scheme 1 presents the suggested mechanism of fracturing of the MoO₃ microparticles to give the nanorods, along with the corresponding SEM images. α-MoO₃ features distorted [MoO₆] octahedra that share four corners to form a plane, with pairs of planes joined together by sharing octahedral edges along the [001] direction. All of these bilayers stack up along the [010] direction, stabilized through weak van der Waals forces (Fig. S1, ESI†). The rates of planar growth along the axes of the α-MoO₃ crystal follow the sequence {001}, {100}, {010}. Among them, {010} is the most stable with the largest exposed surface, while {001} and {100} are unsaturated; accordingly, it is highly favorable for an α-MoO₃ crystal to fracture along the [001] direction, forming belt-like structures.[15,32,33] Therefore, bond breaking along the [001] direction consumes less energy because only one MoO bond connects the corner-shared octahedral, while the two MoO bonds connected along the [100] direction require more energy to break. Hence, particle fragmentation resulted from the capture of particles inside zones experiencing strong stress when the two grinding beads collided (frontal collisions in straining regions or oblique collisions induced by a local shear).[1,34]

The pulling force readily disrupted the weak van der Waals interactions between layers, resulting in a single layer, or a few layers, of smaller size being peeled away. On the other hand, if fractional forces exceeded the mechanical strength of the sheet along the preferred [001] direction, energy-minimization favored one-dimensional shapes, as observed in microscopy images [Scheme 1 and Fig. S9 ESI†] that clearly reveal the fracturing process. The HRTEM image of a fractured sheet

reveals a structure having [001] crystallographic orientation (Fig. S6, ESI†), consistent with the SAED pattern (inset of Fig. 3) recorded along the (001) zone axis. The (110) direction of the SAED pattern is parallel to the rod axis, suggesting that fracturing occurred along the (001) direction. Rupture along the axial direction of the nanosheets occurred much more readily; distortion of octahedra was responsible for the appearance of the resulting rough surfaces, as revealed in the TEM, SEM, and AFM images [Fig. 2 and S6 ESI†]. After only 15 min of imposing pristine MoO_3 to the fractional force, some nanorods were already apparent. Prolonging the imposing time to 90 min resulted in almost all of the pristine MoO_3 microparticles being converted to nanorods (Fig. 3). In addition, the decrease in the microparticles' size to form nanorods was clearly evident from the blue shift of the dispersion (inset of Fig. 3) and the change in powder color (Fig. S2, ESI†) from light to dark blue.

In view of the great promise of α-MoO_3 in lithium storage, we also investigated the electrochemical lithium storage properties of these nanorods as multifunctional electrodes. Overall, the electrochemical route for the lithium storage reaction in α-MoO_3 nanorods can be described[35] as

$$MoO_3 + xLi^+ + xe^- \rightarrow Li_xMoO_3 \tag{1}$$

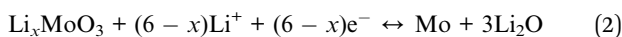$$Li_xMoO_3 + (6-x)Li^+ + (6-x)e^- \leftrightarrow Mo + 3Li_2O \tag{2}$$

Fig. 4a displays charge/discharge voltage profiles for the MoO_3 cathode samples during the first cycle. The discharge curves began with a small plateau near 3.4 V, corresponding to the irreversible process; a more-prominent plateau then occurred at 2.6 V, representing the dominant lithium intercalation process. At the end of the first discharge, the nanorods could deliver a capacity as high as 311 mA h g^{-1}, whereas that of the bulk MoO_3 was only 115 mA h g^{-1}. The subsequent charge

capacities were 315 and 116.5 mA h g^{-1}, leading to irreversible capacity losses of only 1.3%, for both the nanorods and the bulk material, respectively. Thus, the nanorods provided a higher initial capacity, presumably because of their much shorter diffusion length, allowing more efficient insertion/deinsertion of lithium ions.[30] Moreover, the nanorods had a higher specific surface area, which may have provided more lithium insertion sites during the charge/discharge cycles, contributing to its better lithium storage properties. The surface area measurements showed that the surface area of MoO_3 nanorods (20 (m^2 g^{-1})) is higher as compared to the bulk MoO_3 (11 (m^2 g^{-1})). This change in surface area after conversion is indicative of the size reduction accompanying structural rearrangement. Fig. 4b shows the cycling behavior at charge/discharge rates of up to 2000 mA g^{-1}. Although we observed a drop in capacity for both the nanorods and the bulk material, the former could deliver a higher capacity (170 mA h g^{-1}) relative to that for the bulk material (80 mA h g^{-1}) at a rate of 40 mA g^{-1}. Upon gradually increasing the current rate, it became apparent that the nanorods provided much better lithium storage capability than did the bulk material. We attribute the large capacity loss mainly to the irreversible intercalation of lithium ions into the crystal lattice and the formation of Li_2O, as well as other irreversible processes (*e.g.*, inevitable formation of a solid-electrolyte interface layer and electrolyte decomposition) that are common for most transition metal oxides and can be readily mitigated by prelithiation of the electrode for practical use.[12,15]

The charge/discharge and cycling behaviors of the MoO_3 anode samples at 50 mA g^{-1} revealed the same relative electroactivity, with the performance of the nanorods being better than that of the pristine α-MoO_3, along with a rapid decay in capacity (Fig. S10, ESI†). A sharp decrease in cell capacity can be retained using various approaches. For example, Wang *et al.* reported that bio-derived sodium alginate has emerged as the
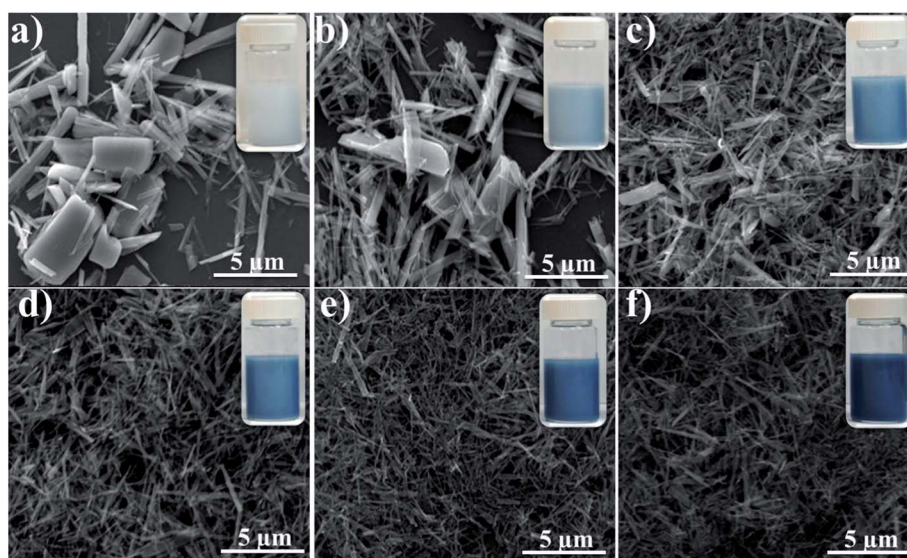

Fig. 3 SEM images of the samples obtained at various time intervals [(a) 15, (b) 30, (c) 45, (d) 60, (e) 75, and (f) 90 min] during the conversion of the 3D bulk MoO_3 material into fractured 2D nanosheets and then into 1D nanorods. Insets: photographs of dispersions of the MoO_3 materials at each conversion stage.
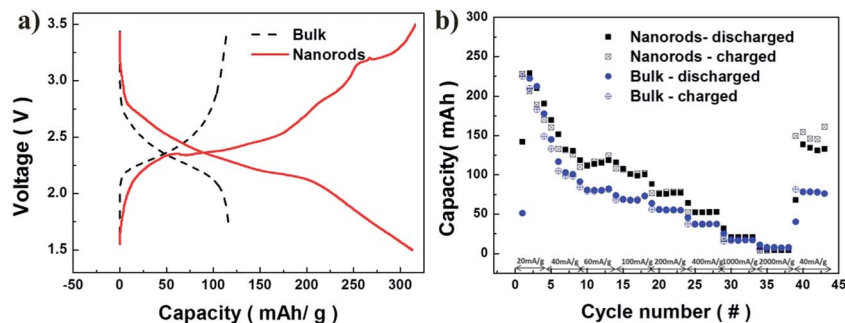
Fig. 4 LIB test: (a) first-cycle charge/discharge voltage profiles at 30 mA g^{-1}; (b) charge/discharge behavior at various current rates. Measurements made with a voltage window of 1.5–3.8 V.

best performing binder for composite α-MoO$_3$ electrodes, providing a stable specific capacity of approximately 800 mA h g^{-1}.[15,36] Tang et al. demonstrated that rechargeable LIBs based on α-MoO$_3$ composite electrodes have excellent retention rates and energy densities, potentially suitable for large power systems.[38] Sen and Mitra found that MoO$_3$ nanobelt composite samples cast on stainless-steel substrates exhibit better electrochemical performance toward Li than do those cast on aluminum (Al) or nickel (Ni) substrates.[29] The highest electrochemical performance to date has been achieved using carbon- and graphite-coated α-MoO$_3$ composites.[5,37]

Conclusion

In summary, we have prepared uniform α-MoO$_3$ nanorods in high yield through a simple, one-step method employing mechanical force, the impact of which fractured the microparticles along the favorable crystal direction such that the resultant nanorods exhibited single-crystalline growth along the [001] direction. These α-MoO$_3$ nanorods displayed higher initial capacity, lower initial irreversible loss, and improved rate behavior, relative to those of the pristine MoO$_3$ microparticles, when used as multifunctional LIB electrodes. The great improvement in lithium storage capability presumably arose from the smaller sizes, greater specific surface areas, and possibly different surface chemistries of the nanorod samples; these features, together with the insertion/extraction mechanism, require further in-depth investigations. This very simple preparation technique has the potential for scaling up to mass production at low cost, offering a promising opportunity to produce nanomaterials in the volumes required for real-world applications.

Acknowledgements

References

1 B. Hu, L. Mai, W. Chen and F. Yang, ACS Nano, 2009, 3, 478–482.

2 Q. Zhang, E. Uchaker, S. L. Candelaria and G. Cao, Chem. Soc. Rev., 2013, 42, 3127–3171.

3 S. Balendhran, S. Walia, H. Nili, J. Z. Ou, S. Zhuiykov, R. B. Kaner, S. Sriram, M. Bhaskaran and K. Kalantar-zadeh, Adv. Funct. Mater., 2013, 23, 3952–3970.

4 D. D. Yao, J. Z. Ou, K. Latham, S. Zhuiykov, A. P. O'Mullane and K. Kalantar-zadeh, Cryst. Growth Des., 2012, 12, 1865–1870.

5 L. Q. Mai, B. Hu, W. Chen, Y. Y. Qi, C. S. Lao, R. S. Yang, Y. Dai and Z. L. Wang, Adv. Biomater., 2007, 19, 3712–3716.

6 Y. Ren, Z. Ma and P. G. Bruce, Chem. Soc. Rev., 2012, 41, 4909–4927.

7 H. Wang and H. Dai, Chem. Soc. Rev., 2013, 42, 3088–3113.

8 M. B. Rahmani, S. H. Keshmiri, J. Yu, A. Z. Sadek, L. Al-Mashat, A. Moafi, K. Latham, Y. X. Li, W. Wlodarski and K. Kalantar-zadeh, Sens. Actuators, B, 2010, 145, 13–19.

9 H. C. Zeng, Inorg. Chem., 1998, 37, 1967–1973.

10 J. Wang, K. C. Rose and C. M. Lieber, J. Phys. Chem. B, 1999, 103, 8405–8409.

11 J. N. Yao, K. Hashimoto and A. Fujishima, Nature, 1992, 355, 624–626.

12 F. F. Ferreira, T. G. S. Cruz, M. C. A. Fantini, M. H. Tabacniks, S. C. de Castro, J. Morais, A. de Siervo, R. Landers and A. Gorenstein, Solid State Ionics, 2000, 136–137, 357–363.

13 J.-H. Huang, T.-Y. Huang, H.-Y. Wei, K.-C. Ho and C.-W. Chu, RSC Adv., 2012, 2, 7487–7491.

14 K. Krauß, A. Drochner, M. Fehlings, J. Kunert and H. Vogel, J. Mol. Catal. A: Chem., 2000, 162, 413–422.

15 Z. Wang, S. Madhavi and X. W. Lou, J. Phys. Chem. C, 2012, 116, 12508–12513.

16 S. M. Paek, J. H. Kang, H. Jung, S. J. Hwang and J. H. Choy, Chem. Commun., 2009, 7536–7538.

17 K. Dewangan, N. N. Sinha, P. K. Sharma, A. C. Pandey, N. Munichandraiah and N. S. Gajbhiye, CrystEngComm, 2011, 13, 927–933.

18 J. Zhou, S. Z. Deng, N. S. Xu, J. Chen and J. C. She, Appl. Phys. Lett., 2003, 83, 2653–2655.

19 S. Hu and X. Wang, J. Am. Chem. Soc., 2008, 130, 8126–8127.

20 J. S. Chen, Y. L. Cheah, S. Madhavi and X. W. Lou, J. Phys. Chem. C, 2010, 114, 8675–8678.

21 K. Kalantar-zadeh, J. Tang, M. Wang, K. L. Wang, A. Shailos, K. Galatsis, R. Kojima, V. Strong, A. Lech, W. Wlodarski and R. B. Kaner, *Nanoscale*, 2010, **2**, 429–433.

22 L. Fang, Y. Shu, A. Wang and T. Zhang, *J. Phys. Chem. C*, 2007, **111**, 2401–2408.

23 X. W. Lou and H. C. Zeng, *Chem. Mater.*, 2002, **14**, 4781–4789.

24 L. Noerochim, J.-Z. Wang, D. Wexler, Z. Chao and H.-K. Liu, *J. Power Sources*, 2013, **228**, 198–205.

25 M. A. Ibrahem, H.-Y. Wei, M.-H. Tsai, K.-C. Ho, J.-J. Shyue and C. W. Chu, *Sol. Energy Mater. Sol. Cells*, 2013, **108**, 156–163.

26 P. A. Spevack and N. S. McIntyre, *J. Phys. Chem.*, 1992, **96**, 9029–9035.

27 C. V. Subba Reddy, Z. R. Deng, Q. Y. Zhu, Y. Dai, J. Zhou, W. Chen and S. I. Mho, *Appl. Phys. A: Mater. Sci. Process.*, 2007, **89**, 995–999.

28 B. Qi, X. Ni, D. Li and H. Zheng, *Chem. Lett.*, 2008, **37**, 336–337.

29 U. K. Sen and S. Mitra, *RSC Adv.*, 2012, **2**, 11123–11131.

30 X.-Y. Xue, Z.-H. Chen, L.-L. Xing, S. Yuan and Y.-J. Chen, *Chem. Commun.*, 2011, **47**, 5205–5207.

31 D. D. Yao, M. R. Field, A. P. O'Mullane, K. Kalantar-zadeh and J. Z. Ou, *Nanoscale*, 2013, **5**, 10353–10359.

32 F. Li and Z. Chen, *Nanoscale*, 2013, **5**, 5321–5333.

33 L. Cheng, M. Shao, X. Wang and H. Hu, *Chem. – Eur. J.*, 2009, **15**, 2310–2316.

34 M. P. Mitoraj and A. Michalak, *Struct. Chem.*, 2012, **23**, 1369–1375.

35 L. A. Riley, S.-H. Lee, L. Gedvilias and A. C. Dillon, *J. Power Sources*, 2010, **195**, 588–592.

36 Y. Sun, J. Wang, B. Zhao, R. Cai, R. Ran and Z. Shao, *J. Mater. Chem. A*, 2013, **1**, 4736–4746.

37 M. F. Hassan, Z. P. Guo, Z. Chen and H. K. Liu, *J. Power Sources*, 2010, **195**, 2372–2376.

38 W. Tang, L. Liu, Y. Zhu, H. Sun, Y. Wu and K. Zhu, *Energy Environ. Sci.*, 2012, **5**, 6909–6913.